



# Chemically bonded Mn<sub>0.5</sub>Cd<sub>0.5</sub>S/BiOBr S-scheme photocatalyst with rich oxygen vacancies for improved photocatalytic decontamination performance



Shijie Li <sup>a,\*</sup>, Changjun You <sup>a</sup>, Ke Rong <sup>a</sup>, Chunqiang Zhuang <sup>b</sup>, Xiaobo Chen <sup>c</sup>, Bin Zhang <sup>a,\*\*</sup>

<sup>a</sup> Key Laboratory of Health Risk Factors for Seafood of Zhejiang Province, National Engineering Research Center for Marine Aquaculture, College of Food Science and Pharmacy, Zhejiang Ocean University, Zhoushan 316022, China

<sup>b</sup> Institute of Microstructure and Property of Advanced Materials, Faculty of Materials and Manufacturing, Beijing University of Technology, Beijing 100124, China

<sup>c</sup> Department of Chemistry, University of Missouri, Kansas City, MO 64110, USA

## ARTICLE INFO

### Keywords:

Mn<sub>0.5</sub>Cd<sub>0.5</sub>S/BiOBr  
Chemically bonded S-Scheme  
Internal electric field  
Oxygen vacancies  
Antibiotic removal  
Photocatalysis

## ABSTRACT

Devising exceptional S-scheme heterojunction photocatalysts utilized in annihilating pharmaceuticals and chromium contamination is significant for addressing the problem of global water pollution. In this work, a chemically bonded Mn<sub>0.5</sub>Cd<sub>0.5</sub>S/BiOBr S-scheme heterostructure with oxygen vacancies is ingeniously developed through a facile *in-situ* solvothermal synthesis. The designed Mn<sub>0.5</sub>Cd<sub>0.5</sub>S/BiOBr heterojunction exhibits eminently reinforced photo-activity for destruction of tetracycline hydrochloride and Cr(VI) as compared with its individual components. This substantial photo-redox performance amelioration is benefitted from the creation of an intense internal electric field (IEF) via supplying powerful driving force and migration highway by interfacial chemical bond to foster the S-scheme electron/hole disintegration. More intriguingly, the IEF at the hetero-interface drives the fast consumption of the photo-induced holes in Mn<sub>0.5</sub>Cd<sub>0.5</sub>S by the photoelectrons from BiOBr, profoundly boosting the enrichment of active photo-carriers and sparing the photo-corrosion of Mn<sub>0.5</sub>Cd<sub>0.5</sub>S. Furthermore, Mn<sub>0.5</sub>Cd<sub>0.5</sub>S/BiOBr with exceptional anti-interference property can work efficiently in real water matrices. Multiple uses of the recycled Mn<sub>0.5</sub>Cd<sub>0.5</sub>S/BiOBr evidence its prominent robustness and stability. This achievement indicates the vast potential of chemically bonded S-scheme photosystems with structural defects in the design of photo-responsive materials for effective wastewater treatment.

## 1. Introduction

With the advancement of the pharmaceutical, agricultural, and chemical sectors, there has been an escalation in the discharge of hazardous pollutants such as refractory pharmaceuticals and heavy metals into aquatic ecosystems. This alarming trend has resulted in global environmental predicaments, jeopardizing ecological equilibrium, and human health [1–4]. To combat this issue, a multitude of techniques have been devised to eliminate these contaminants, namely physical adsorption, biodegradation, photocatalysis, and electrocatalysis [5–9]. Among them, sunlight-triggered catalysis stands out as a sustainable, cost-effective, and efficacious technology for environmental purification by harnessing infinite sunlight as an energy source [10–14]. To promote its industrialization, it is of eminent importance to devise exceptional photocatalysts that can perform effectively and durably during treatment

[15–22].

Among the plethora of available photoactive materials, bismuth-based materials emerge as a class of distinctive photocatalysts due to their low cost, adjustable architecture, and favorable sunlight response. BiOBr stands out as an illustrious visible-light active photocatalyst with several advantages including a favorable band configuration, exceptional photo-oxidative capacity, distinctive 2D architecture, ecological compatibility, abundant resources, and robust durability [23,24]. Despite its inherent virtues, BiOBr faces certain limitations, namely its relatively inferior overall photocatalytic efficacy, attributed to the constrained absorption of visible light and sluggish photo-carrier diffusion and segregation [25,26].

Recent researches demonstrate that the 3D hierarchical architecture of photocatalysts featured by large surface area and high porosity may reinforce the sunlight utilization, foster the exposure of available reactive

\* Corresponding author.

\*\* Corresponding author.

E-mail addresses: [lishijie@zjou.edu.cn](mailto:lishijie@zjou.edu.cn) (S. Li), [zhangbin@zjou.edu.cn](mailto:zhangbin@zjou.edu.cn) (B. Zhang).

and restrain the agglomeration of the catalyst, thus effectively upgrading the photo-activity [27,28]. Furthermore, building heterostructured photocatalyst is a fashionable tactics to advance photoreaction kinetics [19,29–39]. Especially, S-scheme heterostructures have unveiled their tremendous potential in expediting spatial electron/hole segregation and upholding optimal photo-redox power [40–54]. Nonetheless, in most of the developed S-scheme systems, physical contact without chemically bonding hetero-interface between the two components, which is insufficiently interactive, generally results in an unsatisfactory charge migration passage [41,46,52]. In our previous research, the designed  $\text{Bi}_2\text{WO}_6/\text{C}_3\text{N}_4$ /carbon fibers also suffer from unsatisfactory catalytic performance due to the non-chemically bonded hetero-interface [55]. Accordingly, devising chemically bonded S-scheme heterojunction is more appealing because the interfacial chemical bond can function as atomic-level photo-carrier diffusion highway, thereby contributing to prominent photo-activity advancement.

Recently,  $\text{Mn}_{0.5}\text{Cd}_{0.5}\text{S}$  solid solution, comprising a combination of  $\text{CdS}$  and  $\text{MnS}$ , has presented an exceptional level of photocatalytic activity [56,57]. Nonetheless, the limited efficacy and vulnerability to photo-corrosion have imposed constraints on its application potential in photocatalytic reactions [58–60]. Thanking to the relatively negative conduction band (CB) position,  $\text{Mn}_{0.5}\text{Cd}_{0.5}\text{S}$  can serve as an alluring photo-reduction component to incorporate with the  $\text{BiOBr}$  for building S-scheme heterostructure.

Herein, a flower-like  $\text{Mn}_{0.5}\text{Cd}_{0.5}\text{S}/\text{BiOBr}$  S-scheme heterojunction with interfacial chemical bonds and oxygen vacancies (OVs) is

synthesized through a simple solvothermal route.  $\text{Mn}_{0.5}\text{Cd}_{0.5}\text{S}/\text{BiOBr}$  presents a hierarchical 0D/3D heterostructure with zero-dimensional (0D)  $\text{Mn}_{0.5}\text{Cd}_{0.5}\text{S}$  pinning on the surface of three-dimensional (3D)  $\text{BiOBr}$  microspheres. Under the synergistic cooperation of S-scheme heterostructure, interfacial chemical bonds and OVs,  $\text{Mn}_{0.5}\text{Cd}_{0.5}\text{S}/\text{BiOBr}$  displays exceptional photocatalytic properties toward Cr (VI) reduction and tetracycline hydrochloride oxidation under visible light irradiation. This research opens up the exploration of chemically bonded S-scheme system with defects for effective water purification.

## 2. Results and discussion

### 2.1. Characterization

The MCS/BOB photocatalyst was synthesized by a solvothermal method (Fig. 1a). The microstructures of BOB and MCS/BOB photocatalysts were studied by scanning electron microscopy (SEM) and transmission electron microscopy (TEM) (Fig. 1b–h). BOB presents a flower configuration with a diameter ranging from  $\sim 3$  to  $\sim 6 \mu\text{m}$ , consisting of interlaced two-dimensional (2D) nanosheets (Fig. 1b), while MCS has a nanoparticle-like morphology with a size of  $\sim 10$ – $60 \text{ nm}$  (Fig. 1c). After MCS is incorporated with BOB, numerous MCS nanoparticles (NPs) are imbedded into BOB microspheres, creating a dense 0D/3D heterostructure with intense interfacial interaction (Fig. 1d–f). Moreover, the lattice spacings of MCS/BOB are 0.28, and 0.30 nm, belonging to the (102) facet of BOB, and (101) facet of MCS, respectively,

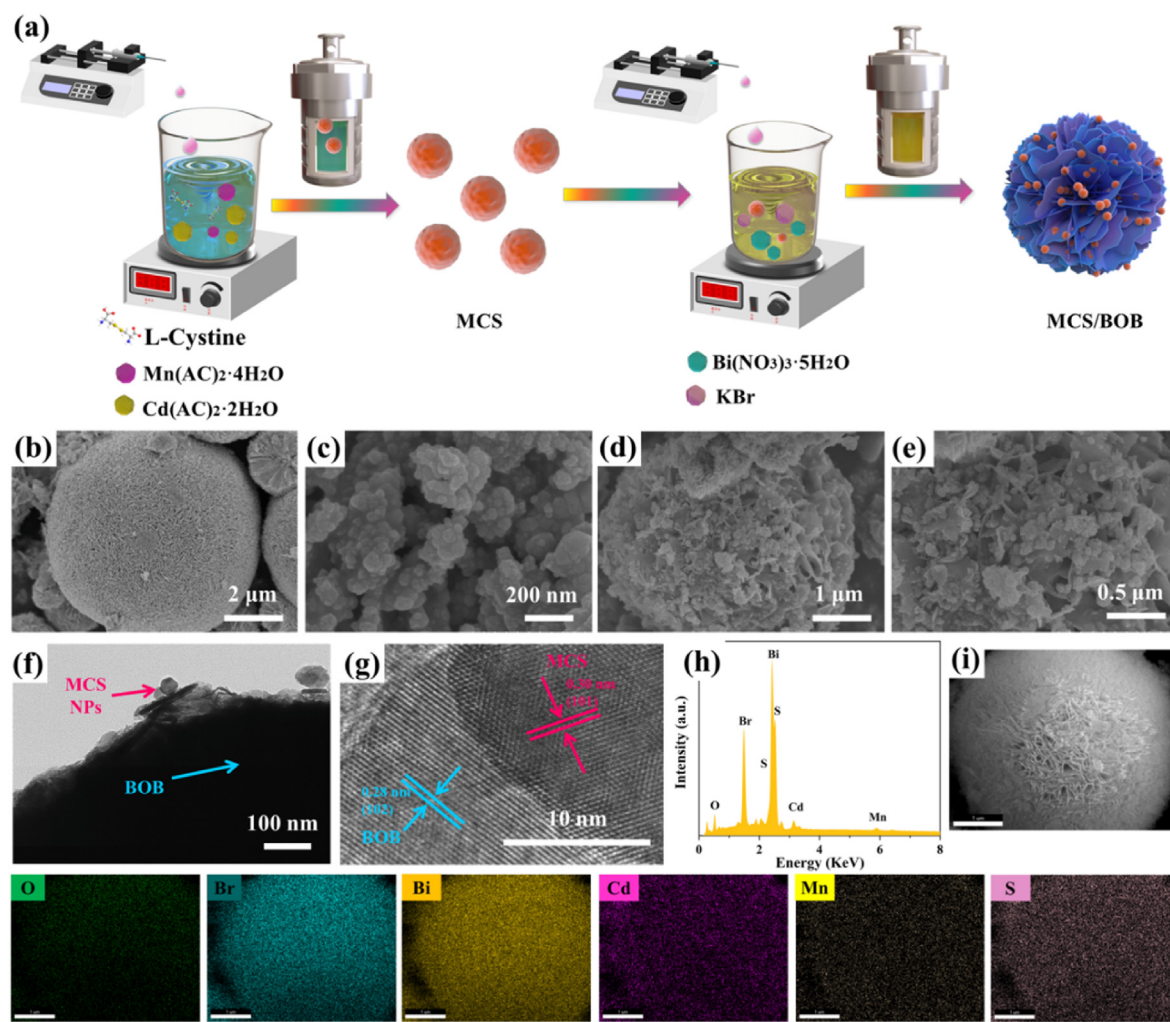


**Fig. 1.** (a) A schema of the synthetic process of MCS/BOB; (b–e) SEM images of BOB (b), MCS (c), and MCS/BOB-2 (d, e); (f–i) TEM image (f), HR-TEM image (g), and EDX spectrum and mapping (h, i) of MCS/BOB-2.

as derived from the HR-TEM image (Fig. 1g). It is worth mentioning that there is compact contact between the two phases of MCS and BOB (Fig. 1g), which is conducive to efficaciously boosting spatial charge segregation in the interfacial region. Corresponding EDX and mapping images (Fig. 1h and i) disclose the uniform attachment of MCS NPs on the hierarchical BOB sphere, which coincides with the SEM and TEM analysis (Fig. 1d–g).

X-ray powder diffraction (XRD) patterns of MCS, BOB, and MCS/BOB heterojunctions were recorded to define their crystal phases (Fig. 2a). The crystalline phases of MCS matches well with hexagonal MnS (JCPDS Card 40-1289) and CdS (JCPDS Card 41-1049) [58]. BOB is identified as tetragonal phases (JCPDS Card 09-0393) [43]. The peaks of MCS/BOB-1 and MCS/BOB-2 are assigned to tetragonal BOB phase without MCS signals identified, due to the low loading content of MCS. As the MCS/BOB mass ratio rises to the 30%, the emergence of emblematic peaks of MCS is ascertained in MCS/BOB-3, reflecting the well incorporation of MCS and BOB via an in-situ solvothermal synthesis.

Fourier transform infrared spectroscopy (FT-IR) measurement was conducted to inspect the structures of MCS/BOB (Fig. S1). The FT-IR spectrum of BOB manifests the stretching bands of Bi–O and Bi–Br at 553, and 1382 cm<sup>-1</sup>, respectively [42,43,61]. MCS/BOB-2 unveils the emblematic absorption peaks of MCS and BOB. Besides, there is weak band at 612 cm<sup>-1</sup> assigned to the Bi–S coordination bond [61,62]. The emergence of the Bi–S bond reflects the partial replacement of Br ions by S ions, which helps to expedite photo-carrier diffusion [61,62]. The above analysis implies the creation of MCS/BOB with interfacial Bi–S bond via in-situ solvothermal synthesis. Noticeably, this unique chemically bonded MCS/BOB heterostructure is beneficial for efficient channelization and segregation of photo-carriers at the hetero-interface.

X-Ray photoelectron spectroscopy (XPS) characterization was performed to elucidate the electronic structure of MCS/BOB-2. The XPS full

spectrum evidences that MCS/BOB-2 involves Mn, O, Br, S, Bi, and Cd elements, signifying the successful integration of MCS and BOB (Fig. S2a), which is in line with the finding of EDX and EDX mapping (Fig. 1i). The Bi 4f spectrum of MCS/BOB-2 (Fig. 2b) contains two symbolic peaks (164.2 and 58.9 eV) associated with Bi 4f<sub>5/2</sub> and Bi 4f<sub>7/2</sub> spin orbits [43,63]. Meanwhile, two feeble peaks of MCS/BOB-2 in Fig. 2b at 161.3 and 162.6 eV are derived from S 2p<sub>3/2</sub> and S 2p<sub>1/2</sub> [64, 65]. In Fig. 2c and d, the binding energies (BEs) of MCS/BOB-2 at 404.8, 411.6, 640.5, and 651.9 eV pertain to Cd 3d<sub>5/2</sub> and Cd 3d<sub>3/2</sub> orbitals of Cd<sup>2+</sup> and Mn 2p<sub>3/2</sub> and Mn 2p<sub>1/2</sub> orbitals of Mn<sup>2+</sup>, respectively [52,59]. The satellite peak of Mn<sup>2+</sup> is centered at 644.3 eV. The BEs of O 1s on MCS/BOB-2 at 532.4, 531.2, and 529.6 eV are associated with surface adhered H<sub>2</sub>O, OVs, and lattice oxygen, respectively (Fig. 2e) [1,66,67]. The Br 3d spectrum of MCS/BOB-2 exhibits two peaks at 69.0 and 68.0 eV (Fig. S2b), pertaining to Br 3d<sub>3/2</sub> and Br 3d<sub>5/2</sub> orbitals [42,43,54], respectively. Compared with BOB (MCS), a negative (positive) displacement in the BEs of Br and Bi (Cd, Mn and S) was observed, representing the generation of interfacial Bi–S bond changes the electronic structure of BOB and MCS through the intense interfacial interaction. The intense interfacial interaction and charge rearrangement between BOB and MCS could lead to the constitution of internal electric field (IEF), further promoting orientated charge drift from MCS to BOB in MCS/BOB until the equilibrium of their  $E_f$  values [42]. Furthermore, electron spin resonance (ESR) spectra (Fig. 2f) indicate that OVs deficient BiOBr (D-BOB) and MCS have no OVs or structural defects while BOB and MCS/BOB-2 possess abundant OVs. On the one hand, OVs can function as electron-capturing centers; On the other hand, OVs can endow MCS/BOB with better sunlight absorption and promoted photo-carrier separation. Thus, the presence of OVs is helpful to the reinforcement of photo-activity.

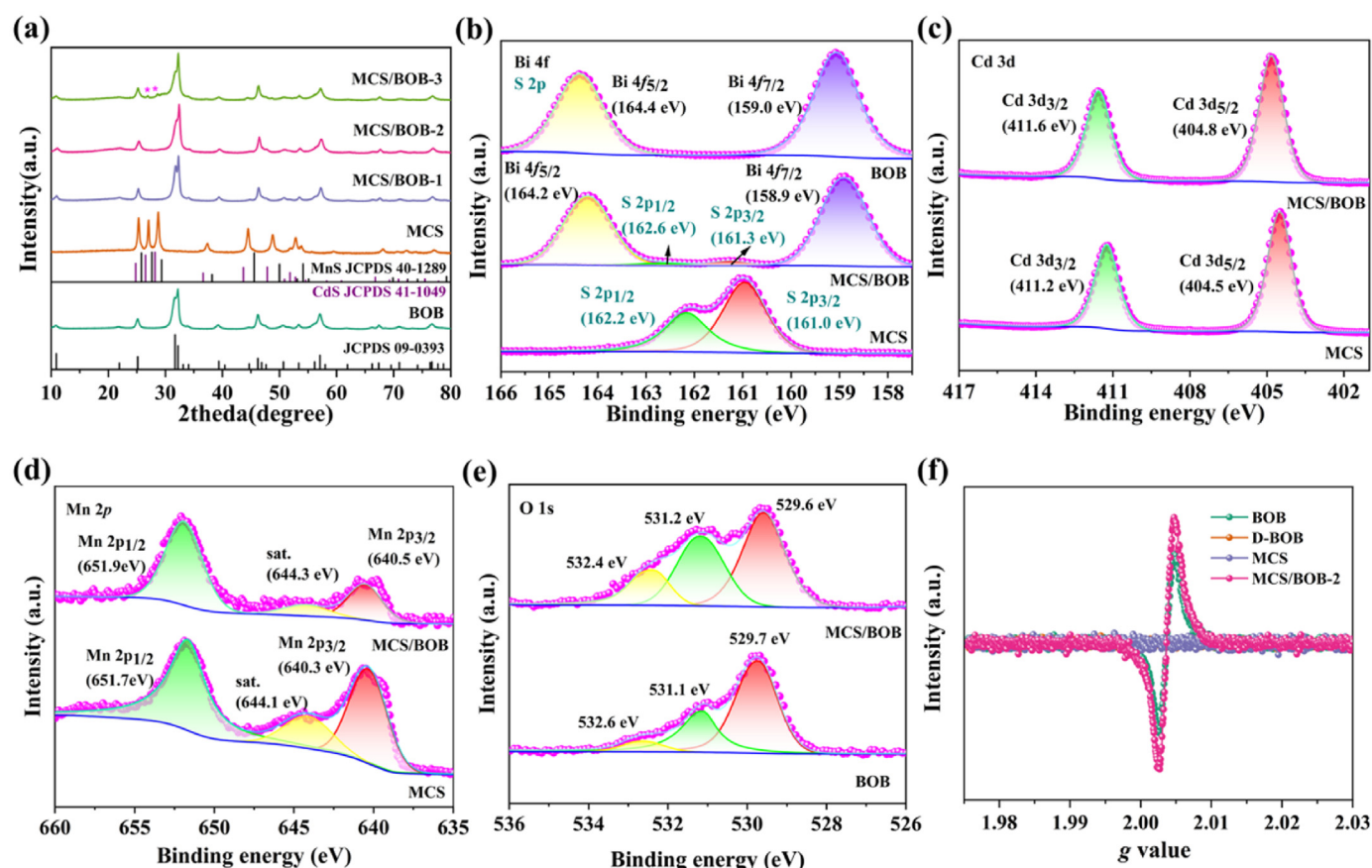


**Fig. 2.** (a) XRD patterns; (b–e) XPS spectra of Bi 4f and S 2p (b), Cd 3d (c), Mn 2p (d), and O 1s (e); (f) ESR spectrum of BOB, D-BOB, MCS, and MCS/BOB-2.

## 2.2. Photocatalytic performance

The photocatalytic efficacy of as-synthesized catalysts was studied by TC destruction under visible light. Dark reaction tests were conducted for 30 min to guarantee that the suspension achieved adsorption-desorption equilibrium before photoreaction. As depicted in Fig. 3a, 15.9%, 15.6%, 21.5%, 25.1%, 20.9%, and 17.4% of TC was adsorbed within 30 min by BOB, MCS, MCS/BOB-1, MCS/BOB-2, MCS/BOB-3, and mixture, respectively. The MCS/BOB heterojunctions exhibit greater adsorption capacity than BOB and MCS, which is helpful to the photo-degradation of contaminants. Next, after 60 min of illumination, TC elimination barely takes places, revealing the stable feature of TC. Pristine BOB and MCS unveil poor TC destruction effectiveness of 62.5% and 44% resulting from their swift photo-carrier reunion. Inspiringly, the incorporation of

BOB and MCS leads to a substantial optimization of the photocatalytic efficacy. The TC destruction rates over MCS/BOB-1, MCS/BOB-2, and MCS/BOB-3 are up to 72.5%, 82.9%, and 73.8%, respectively, highlighting the significance of MCS/BOB S-scheme junction in strengthening the catalytic outcome. Noticeably, the TC decomposition efficacy initially rises and then descends as the content of MCS increases. In fact, establishing a compactly connected interface between MCS and BOB is non-trivial. Excessive MCS may induce the self-aggregation of MCS, which hampers the hetero-interface, compromising the overall catalytic efficacy [42,43]. Moreover, the optimal MCS/BOB-2 manifests appreciably better catalytic efficacy than the mixture, implying that the chemical bond-connected hetero-interface between MCS and BOB makes an eminent contribution to upgrading the photocatalytic efficacy. To highlight the role of OVs in reinforcing the photocatalytic ability of catalysts,

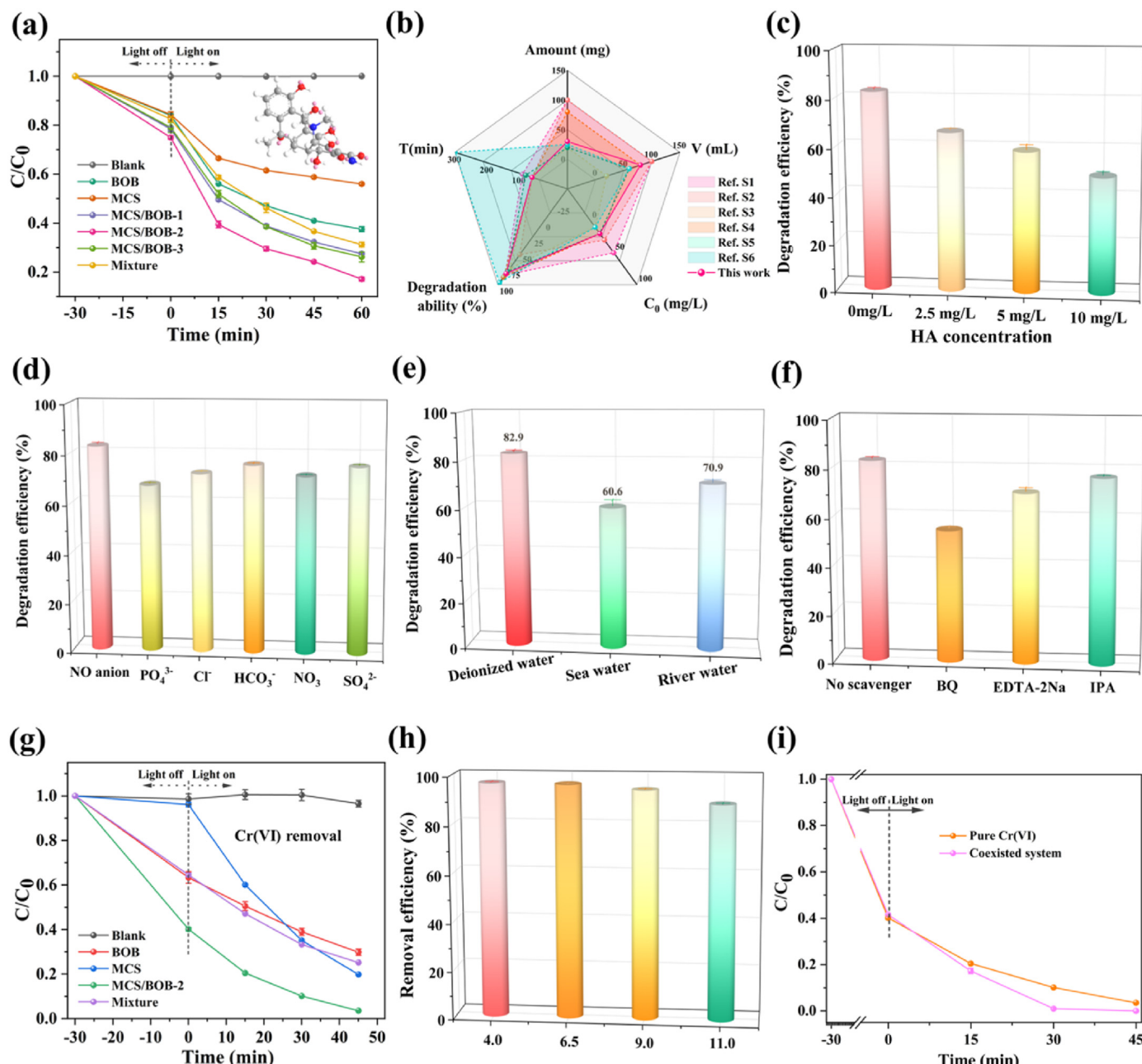


**Fig. 3.** (a) Photocatalytic TC eradication over BOB, MCS, and MCS/BOB series photocatalysts; (b) Comparison of the catalytic performance towards TC removal with the reported catalysts; (c-e) Impact of HA concentration (c), varying ions (d), and various aqueous environments (e) on the destruction of TC by MCS/BOB-2; (f) Trapping experiment of TC degradation over MCS/BOB-2; (g) Photocatalytic Cr(VI) elimination over samples; (h) Photocatalytic Cr(VI) elimination rate at varying pH; (i) Photocatalytic abatement of Cr(VI) in a sole-pollutant system and a co-existence system over MCS/BOB-2.

the catalytic performances of the OVs-deficient D-BOB and MCS/D-BOB were tested. As depicted in Fig. S3a, pristine BOB exhibits higher catalytic effectiveness than D-BOB. Meanwhile, the photoactivity of MCS/BOB-2 is better than that of MCS/D-BOB. Such a result indicates that the OVs are conducive to promoting the catalytic performance. More impressively, the photo-activity of MCS/BOB-2 is superior or comparable to most of the heterojunction photocatalysts (Fig. 3b and Table S1). A kinetic fitting analysis of the degradation curves over MCS/BOB catalysts was implemented and the result is displayed in Fig. S3b. Clearly, the pseudo-first-order rate constant of MCS/BOB-2 is as high as  $0.0229 \text{ min}^{-1}$ , nearly 1.8, 3.6 and 1.4 folds that of BOB ( $0.0128 \text{ min}^{-1}$ ), MCS ( $0.0063 \text{ min}^{-1}$ ) and the mixture ( $0.0161 \text{ min}^{-1}$ ), respectively.

The treatment effectiveness of MCS/BOB-2 in the presence of humic acid (HA) was tested and the result demonstrates that the photo-activity of MCS/BOB-2 is gradually inhibited as increasing the HA concentration, which arises from the occupation of ROS by HA [42]. Overall, MCS/BOB-2 can work effectively in the presence of HA (Fig. 3c). Besides, the photocatalytic outcome of MCS/BOB-2 in the presence of diverse anions was examined (Fig. 3d). The destruction percentages of TC are about 72.3%, 71.6%, 67.5%, 75.5%, and 75.9% when  $\text{Cl}^-$ ,  $\text{NO}_3^-$ ,  $\text{PO}_4^{3-}$ ,  $\text{SO}_4^{2-}$ , and  $\text{HCO}_3^-$  are present, respectively, reflecting the distinguished anion adaptability of MCS/BOB-2. The TC degradation over MCS/BOB-2 under the irradiation of single wavelengths of 500, 550 and 600 nm was further carried out. As shown in Fig. S3c the TC degradation efficiencies over MCS/BOB-2 are up to 70.4%, 55.7%, and 51.1% under the light irradiation wavelengths of 450, 500 and 550 nm, respectively. Frankly, the stability of a photocatalyst is significant for its industrial application [42]. The recycle experiments for TC degradation were implemented to scrutinize the reusability of MCS/BOB-2. Fig. S3d exhibits that the catalytic efficacy of MCS/BOB-2 does not drop sharply during five successive runs, evidencing its strong stability. Moreover, the XRD patterns and SEM image demonstrate that the phases and microstructure of MCS/BOB-2 remain almost unchanged after long-term cycling test, confirming the high structural stability of MCS/BOB-2 (Figs. S3e and f). The photocatalytic TC destruction over MCS/BOB-2 was implemented in real water matrix. Fig. 3e displays that the photocatalytic TC destruction efficacy is inhibited in river (70.9%) and sea water (60.6%) by the interfering substances, which capture ROS resulting in a certain decrement in TC destruction efficiency [42,43].

To uncover the roles of ROS in eliminating TC over MCS/BOB-2, scavenging experiments were implemented by adopting EDTA-2Na, IPA and BQ as quenchers of  $\text{h}^+$ ,  $\bullet\text{OH}$ , and  $\bullet\text{O}_2^-$ , respectively (Fig. 3f). The TC elimination efficiency is 82.9% without addition of a quencher. In comparison, the photocatalytic eradication rate of TC drops by 12.5%, 6% and 28.2% after introducing EDTA-2Na, IPA and BQ, respectively. This fact implies that  $\text{h}^+$  and  $\bullet\text{O}_2^-$  are the prime reactive species involved in TC decomposition.

The photocatalytic Cr(VI) reduction experiments were applied to appraise the photo-reduction efficacy of the MCS/BOB heterojunction. From Fig. 3g, dark reaction tests reveal that MCS/BOB-2 exhibits better Cr(VI) adsorption capacity (59.8%) than BOB (36.7%), MCS (3.9%), and mixture (35.5%). The Cr(VI) photoreaction experiments show that MCS/BOB-2 acquires the highest treatment efficacy, with the Cr(VI) elimination percentage up to 96.5% after 45 min visible-light irradiation. While only 70.2%, 80.2% and 74.8% of Cr (VI) was annihilated by sole BOB, MCS and mixture, respectively. Notably, MCS/BOB-2 achieves the maximum reduction rate constant of ( $0.0534 \text{ min}^{-1}$ ), 3.2 and 1.5 folds that of BOB ( $0.0168 \text{ min}^{-1}$ ) and MCS ( $0.0351 \text{ min}^{-1}$ ), respectively (Fig. S4a). This achievement highlights the superiority of the S-scheme MCS/BOB junction in upgrading the photo-redox behavior [41]. The Cr(VI) photo-reduction test over MCS/BOB-2 at diverse pH value was conducted and the result shows that MCS/BOB-2 works effectively at pH ranging from 4 to 11 and its catalytic performance is slightly compromised in alkaline environments (Fig. 3h), certifying the high adaptability to a broad range of pH environment.

The Cr(VI) photoreduction efficiency of MCS/BOB-2 decreased by

40.7% and 20.3% with the addition of  $\text{AgNO}_3$  and TEMPO (Fig. S4b), proving that the photogenerated  $e^-$  is the major active species in the MCS/BOB-2 system for the Cr(VI) photoreduction.

The robustness of MCS/BOB-2 was also ascertained by the relatively steady efficacy for Cr(VI) removal in recycling experiments (Fig. S5a). Fig. S5b displays that the XRD spectra of MCS/BOB-2 before and after use are almost identical, verifying the remarkable stability of MCS/BOB-2. To unlock the photo-reduction product of Cr(VI) over MCS/BOB-2, the XPS analysis was implemented (Fig. S5c). Evidently, the presence of the emblematic peaks, namely, 586.6 eV ( $\text{Cr } 2\text{p}_{1/2}$ ) and 576.5 eV ( $\text{Cr } 2\text{p}_{3/2}$ ) [41–43], belonging to Cr(III) unveils that the effective photocatalytic reduction of Cr(VI) to Cr(III) is achieved by MCS/BOB-2 during photocatalysis.

The photocatalytic experiments of TC and Cr(VI) in a co-existence (Cr(VI)-TC) system was performed to assess the capability of MCS/BOB-2 to eliminate them concurrently. In the TC-Cr(VI) system, although TC abatement over MCS/BOB-2 is slightly attenuated compared to that in a pure TC environment. The TC elimination rate by MCS/BOB-2 still achieves a high level (Figs. S6a and b). Attractively, the Cr(VI) photo-reduction performance of MCS/BOB-2 is substantially strengthened in the TC-Cr(VI) system, and the corresponding  $k$  is up to  $0.0853 \text{ min}^{-1}$ , about 1.6 folds that ( $0.0534 \text{ min}^{-1}$ ) in a sole Cr(VI) system (Fig. S6c and Fig. 3i). This phenomenon can be explained by the synergistic effect between MCS/BOB-2, Cr(VI), and TC, wherein the TC readily consume the  $\text{h}^+$  of MCS/BOB-2, guaranteeing the efficient photo-carrier disintegration and accumulation of  $e^-$  for Cr(VI) reduction.

### 2.3. TC degradation process and toxicity assessment

The intermediates of TC during reaction were ascertained by LC-MS (Fig. S7, Table S2). The photocatalytic destruction of TC over MCS/BOB proceeded in two routes by oxidation of ROS (Fig. 4a) [55]. In pathway I, the decarbonylation, deamination, demethylation and dehydroxylation happen for producing P1. Afterwards, P1 is decomposed into P2 via ring cleavage. The conversion of P2 into P3 is accomplished via ring opening and bond cleavage reactions. In pathway II, the attack of ROS induces the formation of P4 through demethylation and hydroxyl-ation reactions, which is further transformed into P5 via dehydroxylation etc. Subsequently, the demethylation, deamination, and ring breaking occur, leading to generation of P6. After that, P6 goes through dehydroxylation and decarbonylation reactions to generate P7. As the reaction continues, successive oxidation reactions give birth to P8–P11. Ultimately, the fierce and incessant strike of ROS on TC antibiotic leads to the effective decontamination performance of the catalysts during photocatalysis.

The toxicity evaluation was executed to disclose the potential hazards of these intermediates to human health and aquatic ecosystem (Fig. 4b–d and Table S3). In Fig. 4b, all products except P2 and P5 demonstrate lower mutagenicity compared to TC, and the mutagenicity of P3, P4, and P6–P11 is ascertained to be negative. In Fig. 4c, all intermediates except P2 and P7 exhibit weaker developmental toxicity relative to TC. Fig. 4d uncloses that except P1, the  $\text{LC}_{50}$  of the intermediates for fathead minnow is greater than that of TC, representing a decrement in toxicity. More intriguingly, P4, P6, P8 and P10 are non-toxic chemicals. The toxicological evaluations reveal MCS/BOB holds eminent promise for antibiotic wastewater purification.

### 2.4. Mechanism insights

The optical features of MCS/BOB heterojunctions were detected by UV-vis diffuse reflectance spectroscopy (UV-Vis DRS) (Fig. 5a). BOB displays an absorption edge at 469 nm, in accordance with a  $E_g$  of 2.78 eV [42] (Fig. 5b). Compared with BOB, the MCS/BOB catalysts obtain a notable improvement of sunlight-responsiveness due to the incorporation of MCS with narrowed  $E_g$  of 2.28 eV (Fig. 5b). Clearly, the  $E_g$  values of MCS/BOB-1, MCS/BOB-2 and MCS/BOB-3 are determined as 2.66, 2.69

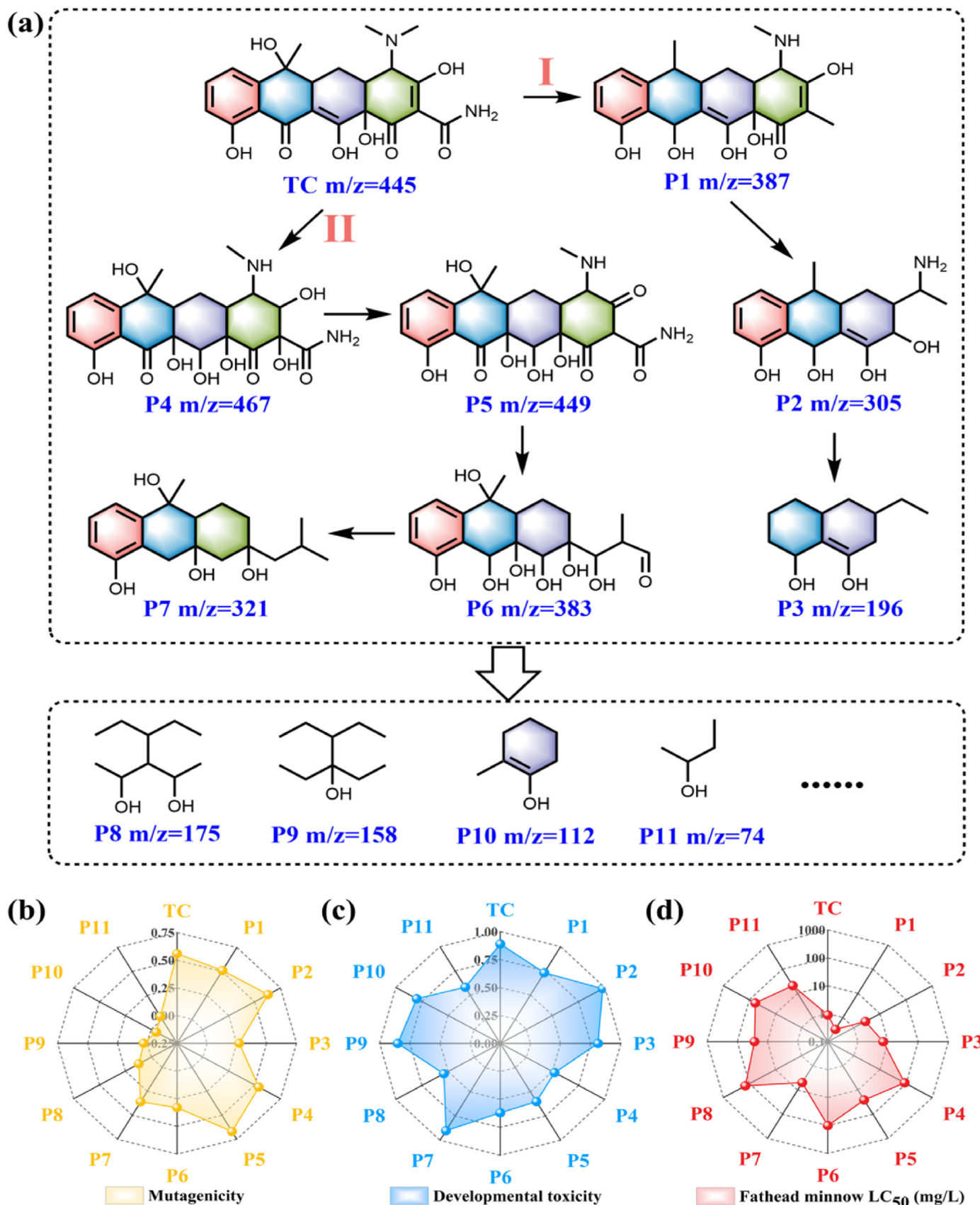
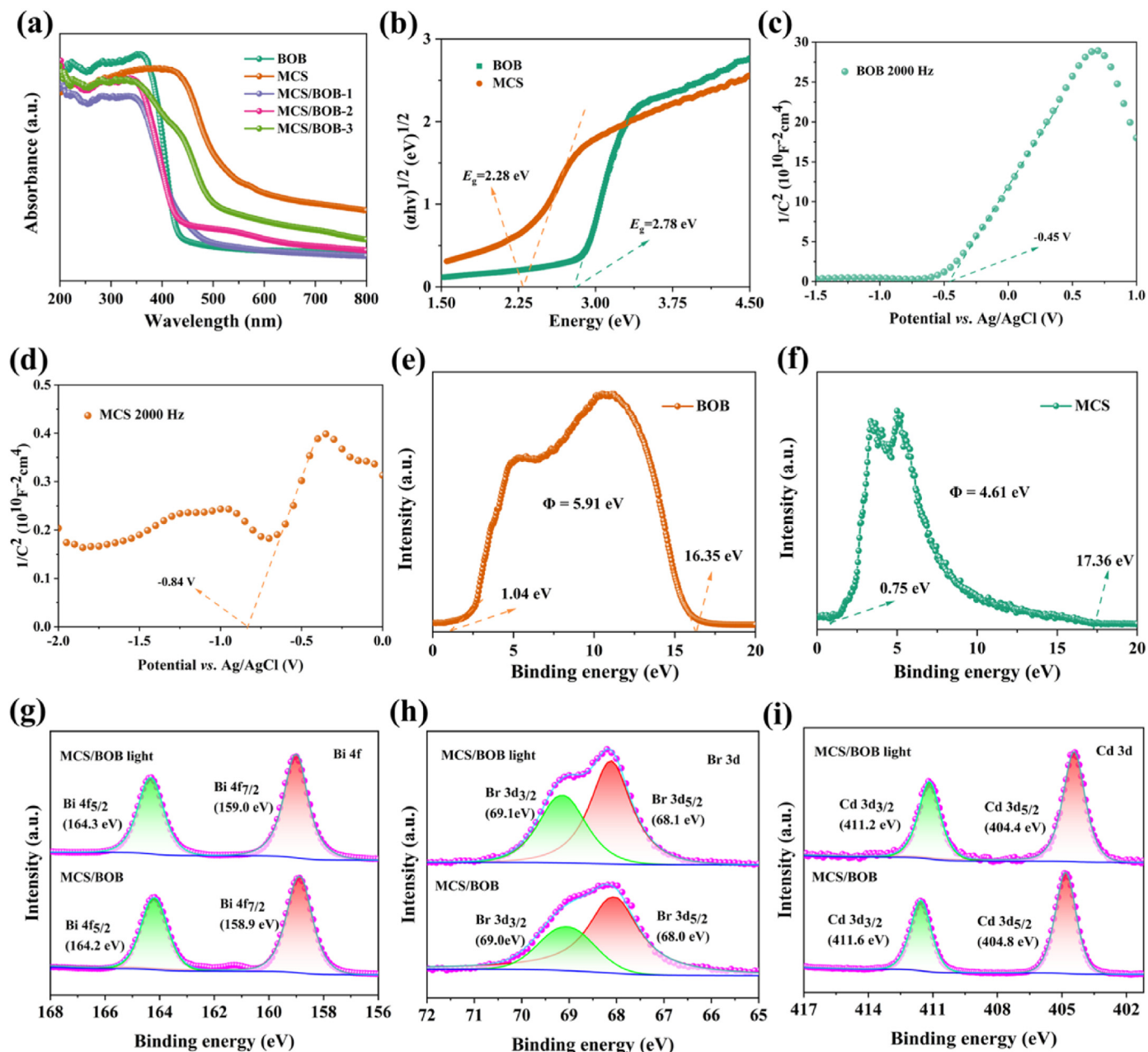


Fig. 4. (a) Plausible destruction routes of TC by MCS/BOB-2; (b-d) Toxicity analysis.



**Fig. 5.** (a) UV-vis DRS patterns; (b) Tauc plots; (c, d) Mott–Schottky data; (e, f) UPS profiles of BOB and MCS; (g–i) XPS spectra of Bi 4f (g), Br 3d (h), and Cd 3d (i) for MCS/BOB-2 conducted in dark and under light illumination, respectively.

and 2.33 eV (Fig. S9). Furthermore, the CB positions ( $E_{\text{CB}}$ ) of BOB and MCS were obtained by Mott–Schottky plots, which are defined as  $-0.35$  and  $-0.74$  V versus NHE, respectively (Fig. 5c and d). Correspondingly, the  $E_{\text{VB}}$  of BOB and MCS were determined to be  $2.43$  and  $1.54$  V versus NHE, respectively, by means of the equation:  $E_{\text{g}} = E_{\text{VB}} - E_{\text{CB}}$ .

For a deeper comprehension of the specific charge transport course at the MCS/BOB hetero-interface, ultraviolet photoelectron spectroscopy (UPS) analysis was performed to uncloze the work functions ( $\Phi$ ) of MCS and BOB. UPS measurements disclose that the  $\Phi$  values of MCS and BOB are determined to be  $4.61$  and  $5.91$  eV, respectively (Fig. 5e and f), by referring to the formula:  $\Phi = h\nu - (E_{\text{cutoff}} - E_{\text{fermi}})$ . Further, the  $E_{\text{f}}$  values are estimated to be  $4.61$  and  $5.91$  eV for MCS [58] and BOB [42,68], respectively, according to the equation:  $E_{\text{f}} = -\Phi$ . Evidently, the higher  $\Phi$  and lower  $E_{\text{f}}$  of BOB than MCS certifies the charge migration from MCS to BOB before light illumination, which coincides with the XPS analysis (Fig. 2b–e). Such charge redistribution propels the phases to achieve the

balanced  $E_{\text{f}}$  and thus creates an IEF in the heterostructure [41,55]. In-situ XPS characterization was performed to confirm the S-scheme photo-carrier drift during photocatalysis (Fig. 5g–i). Evidently, under light irradiation, the BEs of Bi and Br (Cd) in MCS/BOB experience a red (blue) shift (Fig. 5g–i). Such shifts highlight the migration of photo-induced electrons from BOB to MCS under light, confirming the establishment of MCS/BOB S-scheme junction. From the above results, an S-scheme photo-carrier segregation mechanism over MCS/BOB is depicted in Fig. S10.

The textural configurations of MCS, BOB, and MCS/BOB were scrutinized by means of  $\text{N}_2$  adsorption-desorption measurements. Fig. S8 displays that MCS/BOB-2 has the improved surface area of  $\sim 31.8 \text{ m}^2 \text{ g}^{-1}$  compared with MCS ( $22.3 \text{ m}^2 \text{ g}^{-1}$ ) and BOB ( $23.2 \text{ m}^2 \text{ g}^{-1}$ ). In fact, the large surface area and porous architecture help to foster the formation of reactive regions, the capture and enrichment of contaminants during reaction, leading to strengthened catalytic effectiveness [42].

Photoelectronic measurements were implemented to obtain deep insight into the mechanism of photo-activity reinforcement [42,43,48]. Electrochemical impedance spectroscopy measurement was conducted to appraise the charge transportation resistance of MCS, BOB, and MCS/BOB heterojunctions (Fig. 6a). As shown in the inset image of Fig. 6a, the EIS Nyquist plots were simulated by the equivalent circuit diagram. In this system, the resistance between the fluorine-doped tin

oxide and samples ( $R_1$ ), and the charge drift resistance across the electrolyte/photoanode interface ( $R_2$ ) are displayed in Table S4. In principle, a smaller EIS radius and lower  $R_2$  represent that the transfer resistance of photo-excited electrons is weaker [41,43]. Apparently, MCS/BOB-2 unveils a much smaller semicircle diameter and lower  $R_2$  of 15,547  $\Omega$  as compared with MCS ( $R_2$ , 444,170  $\Omega$ ), BOB ( $R_2$ , 120,470  $\Omega$ ), MCS/BOB-1 ( $R_2$ , 78,849  $\Omega$ ), and MCS/BOB-3 ( $R_2$ , 19,691  $\Omega$ ), reflecting the lowest

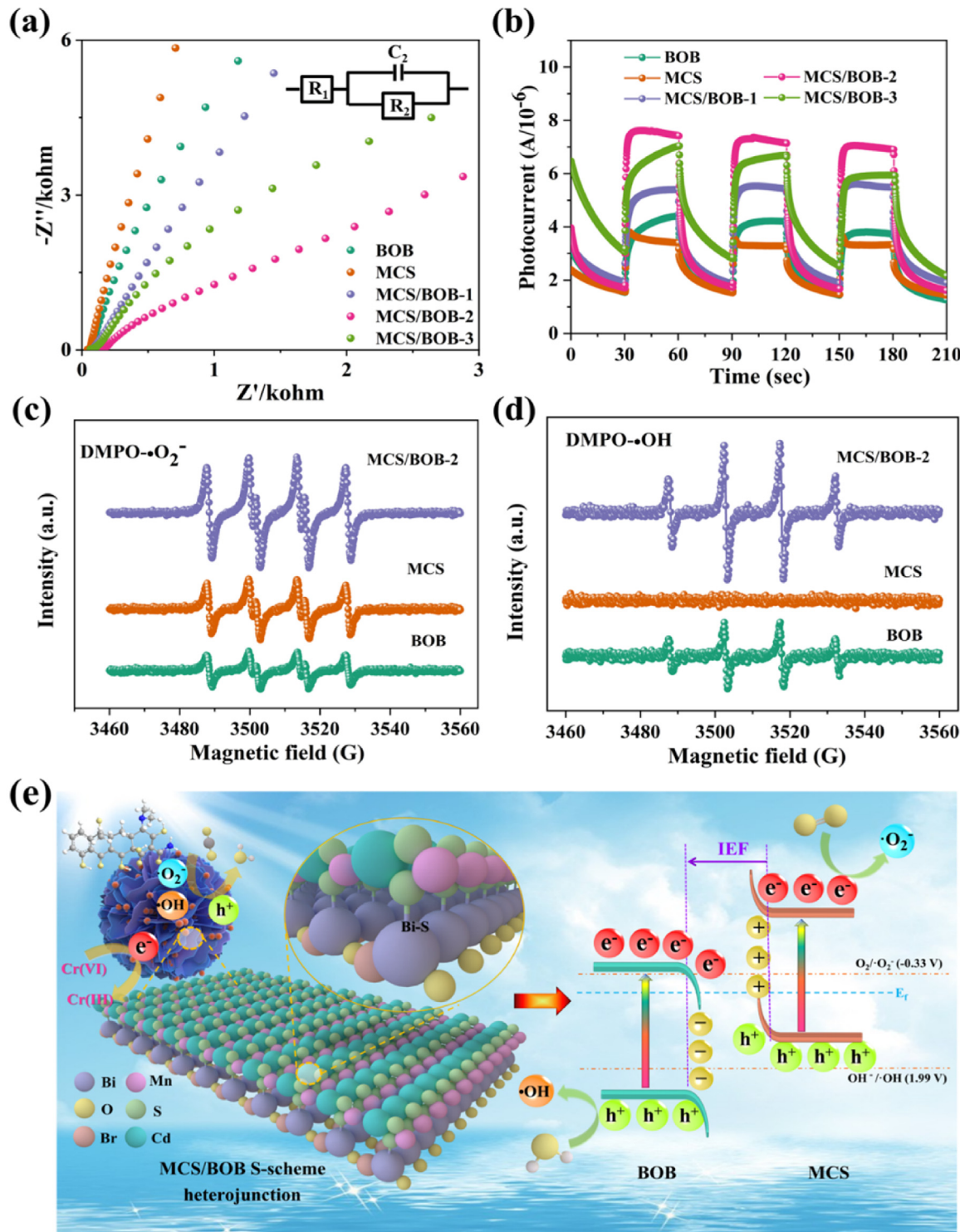


**Fig. 6.** (a-b) EIS profiles (a), and photocurrent responses (b) of BOB, MCS, and MCS/BOB series samples; (c-d) ESR data for MCS, BOB and MCS/BOB-2; (e) The photoreaction mechanism for TC and Cr(VI) eradication by MCS/BOB-2.

charge-migration resistance [42]. The dynamic photo-carrier dissociation behaviors of MCS, BOB, and MCS/BOB heterojunctions were explored by photocurrent response measurement. In Fig. 6b, the MCS/BOB-2 possesses a stronger photocurrent density than BOB, MCS, MCS/BOB-1 and MCS/BOB-3, revealing the most effective generation and detachment of photo-carriers within MCS/BOB-2. In the meantime, PL spectra were also investigated. MCS/BOB-2 has a weaker PL peak intensity compared to BOB, implying the intrinsic better electrons/holes separation rate that MCS/BOB-2 owns (Fig. S11). The results of photo-electronic characterizations and PL measurements verify the cardinal role of chemically bonded S-scheme heterostructure in propelling the photo-carrier detachment.

EPR analyses were executed to authenticate the S-scheme mechanism [4,42,43]. As depicted in Fig. 6c, d, a distinctive reinforcement of the  $\bullet\text{O}_2^-$  signal intensity upon MCS/BOB-2 formation is ascertained, revealing the more effective production of  $\bullet\text{O}_2^-$  is realized by MCS/BOB-2. Besides, the  $\bullet\text{OH}$  signal of MCS was negligible, reflecting its incompetence in creation of  $\bullet\text{OH}$  species resulting from the negative  $E_{VB}$ . MCS/BOB-2 presents an intensified signal of  $\bullet\text{OH}$  relative to BOB, revealing that more high-energetic holes are congregated on MCS/BOB for producing  $\bullet\text{OH}$  species. The EPR analyses corroborate the S-scheme migration course of photo-induced charge-carriers in MCS/BOB-2 driven by the IEF.

These findings convincingly demonstrate that the MCS/BOB heterostructure possesses the unique S-scheme photoinduced-carrier segregation mechanism (Fig. 6e). BOB unveils a greater  $\Phi$  in comparison with MCS. Upon hybridization of MCS and BOB with interfacial Bi-S bonds, electrons transfer from MCS to BOB until their  $E_f$  reach equilibrium. Consequently, such charge movement give birth to an IEF pointing from MCS to BOB at the interface, accompanied by band bending [43]. Under visible light, both MCS and BOB could be photoexcited for creating electrons and holes. The IEF, band bending and Coulomb interaction propel CB electrons of BOB to reunite with the VB holes of MCS through the interfacial Bi-S bonds. In the case, feeble photo-carriers were destroyed so as to retain the high-energetic ones in the system [42]. Such S-scheme charge separation process is not only conducive to spatial detachment of photo-carriers, but can also conserve the maximum redox ability of the integrated system. Of note, the interfacial chemical bond in the MCS/BOB heterostructure may function as atomic-level charge transportation passage, favoring the S-scheme charge drift and separation. Meanwhile, the OVs are helpful to fostering the photo-carrier disassociation and the availability of numerous active sites, thus strengthening the photo-redox capability [41,69–72]. Above all, profiting from the synergy of the interfacial Bi-S bond, IEF, S-scheme heterostructure and OVs, the optimal MCS/BOB heterostructure demonstrates superior photo-redox performance towards the decontamination of TC and Cr (VI).

### 3. Conclusions

In summary, an innovative S-scheme photosystem of MCS/BOB with interfacial bond and OVs, constructed by pinning MCS nanoparticles on BOB microflowers, is delicately devised for efficacious decontamination of antibiotic and Cr(VI). The OVs mediated S-scheme system with interfacial Bi-S bond and internal electric field between MCS and BOB reinforces the sunlight responsiveness, promotes the disassociation and segregation of photo-carriers, and maximizes the redox potential, thus strengthening the photocatalytic performance significantly. This discovery demonstrates that combining interfacial chemical bonds and defects modulated S-scheme junction is a promising route for the development of outstanding catalysts for environmental protection.

## 4. Experiment

### 4.1. Catalyst preparation

**Synthesis of  $\text{Mn}_{0.5}\text{Cd}_{0.5}\text{S}$  (MCS):** Initially, 1.442 g of L-cystine was

dispersed into 50 mL deionized water to yield a white suspension by magnetic agitation. Then the pH of the suspension was adjusted to 10.6 using NaOH (6 mol L<sup>-1</sup>). Afterwards, 25 mL of aqueous solution containing 0.266 g  $\text{Cd}(\text{AC})_2 \cdot 2\text{H}_2\text{O}$  and 0.245 g  $\text{Mn}(\text{AC})_2 \cdot 2\text{H}_2\text{O}$  was gradually added while stirring constantly. The resulting mixture was stirred for 1 h before being heated in a 50 mL Teflon-lined autoclave at 130 °C for 10 h. The solid samples were rinsed sufficiently with deionized water and alcohol, and dried at 60 °C overnight.

**Synthesis of  $\text{Mn}_{0.5}\text{Cd}_{0.5}\text{S}/\text{BiOBr}$  (MCS/BOB):** 0.7275 g of  $\text{Bi}(\text{NO}_3)_3 \cdot 5\text{H}_2\text{O}$  and 0.1785 g of KBr were dissolved in 12 mL of ethylene glycol and 24 mL of ethylene glycol-ethanol solution composed of 12 mL of ethylene glycol and 12 mL of ethanol), which were termed as solution A and B, respectively. While stirring, solution B was poured into A to attain transparent liquid C. Next, a weighed amount of MCS was fully suspended in solution C with stirring for 3 h. The mixture loaded into 50 mL Teflon-lined autoclave was reacted at 150 °C for 10 h. The solid samples were efficaciously rinsed with ethanol and deionized water to swap out the solvents before being dried at 65 °C overnight. MCS/BOB-1, MCS/BOB-2, and MCS/BOB-3 samples were obtained with MCS/BOB mass ratios of 5%, 10%, and 30% respectively. For comparison, an OV-deficient BiOBr denoted as D-BOB was also synthesized under the identical condition by replacing ethylene glycol-ethanol solution with deionized water.

### 4.2. Photocatalytic measurements

The photocatalytic decontamination of tetracycline hydrochloride (TC) and Cr(VI) were carried out to probe the catalytic efficacy of the as-created MCS/BOB. Typically, 30 mg of catalysts was placed in TC solution (20 mg/L, 80 mL) or Cr(VI) solution (10 mg/L, 80 mL). The pollutant solution was stirred in dark for 30 min to get homogeneous suspension and make it reach adsorption balance. Subsequently, the irradiation by a 300 W Xe lamp ( $\lambda > 420$  nm) triggers the photoreaction. At each time interval, the solution was taken out for analysis. The TC concentrations were quantified utilizing a UV-vis spectrophotometer at its maximum absorption wavelength of 356 nm. Meanwhile, the Cr(VI) concentrations were tested via the diphenylcarbazid (DPC) approach with spectrophotometer at 540 nm.

### Declaration of competing interest

The authors declare that they have no known competing financial interests or personal relationships that could have appeared to influence the work reported in this paper.

### Acknowledgments

This research has been financially supported by the National Natural Science Foundation of China (U1809214), the Natural Science Foundation of Zhejiang Province (LY20E080014 and LTGN23E080001), and the Science and Technology Project of Zhoushan (2022C41011).

### Appendix A. Supplementary data

Supplementary data to this article can be found online at <https://doi.org/10.1016/j.apmate.2024.100183>.

### References

- [1] R.I. McDonald, P. Green, D. Balk, B.M. Fekete, C. Revenga, M. Todd, M. Montgomery, Urban growth, climate change, and freshwater availability, Proc. Natl. Acad. Sci. USA 108 (2011) 6312–6317.
- [2] R.P. Schwarzenbach, B.I. Escher, K. Fenner, T.B. Hofstetter, C.A. Johnson, U.v. Gunten, B. Wehrli, The challenge of micropollutants in aquatic systems, Science 313 (2006) 1072–1077.
- [3] P. Löffler, B.I. Escher, C. Baduel, M.P. Virta, F.Y. Lai, Antimicrobial transformation products in the aquatic environment: global occurrence, ecotoxicological risks, and potential of antibiotic resistance, Environ. Sci. Technol. 57 (2023) 9474–9494.

- [4] H. Xu, Y. Jia, Z. Sun, J. Su, Q.S. Liu, Q. Zhou, G. Jiang, Environmental pollution, a hidden culprit for health issues, *Eco-Environ. Health* 1 (2022) 31–45.
- [5] A.J.d. Santos, H.L. Barazorda-Ccahuana, G. Caballero-Manrique, Y. Chérémont, P.J. Espinoza-Montero, J.R. González-Rodríguez, U.J. Jáuregui-Haza, M.R.V. Lanza, A. Nájera, C. Oporto, A.P. Parada, T. Pérez, V.D. Quezada, V. Rojas, V. Sosa, A. Thiam, R.A. Torres-Palma, R. Vargas, S. García-Segura, Accelerating innovative water treatment in Latin America, *Nat. Sustain.* 6 (2023) 349–351.
- [6] Y. Liu, K. Wang, Z. Zhou, X. Wei, S. Xia, X.m. Wang, Y.F. Xie, X. Huang, Boosting the performance of nanofiltration membranes in removing organic micropollutants: trade-off effect, strategy evaluation, and prospective development, *Environ. Sci. Technol.* 56 (2022) 15220–15237.
- [7] M. Caban, P. Stepnowski, How to decrease pharmaceuticals in the environment? A review, *Environ. Chem. Lett.* 19 (2021) 3115–3138.
- [8] H. Deng, Y. Tu, H. Wang, Z. Wang, Y. Li, L. Chai, W. Zhang, Z. Lin, Environmental behavior, human health effect, and pollution control of heavy metal(Iloid)s toward full life cycle processes, *Eco-Environ. Health* 1 (2022) 229–243.
- [9] Z. Chen, W. Wei, H. Chen, B.J. Ni, Recent advances in waste-derived functional materials for wastewater remediation, *Eco-Environ. Health* 1 (2022) 86–104.
- [10] L. Peng, H. Wang, G. Li, Z. Liang, W. Zhang, W. Zhao, T. An, Bioinspired artificial spider silk photocatalyst for the high-efficiency capture and inactivation of bacteria aerosols, *Nat. Commun.* 14 (2023) 2412.
- [11] S.K. Loeb, P.J.J. Alvarez, J.A. Brame, E.L. Cates, W. Choi, J. Crittenden, D.D. Dionysiou, Q. Li, G. Li-Puma, X. Quan, D.L. Sedlak, T.D. Waite, P. Westerhoff, J.H. Kim, The technology horizon for photocatalytic water treatment: sunrise or sunset? *Environ. Sci. Technol.* 53 (2019) 2937–2947.
- [12] D. Mateo, J.L. Cerrillo, S. Durini, J. Gascon, Fundamentals and applications of photo-thermal catalysis, *Chem. Soc. Rev.* 50 (2021) 2173–2210.
- [13] J.Y.Y. Loh, G. Sharma, N.P. Kherani, G.A. Ozin, Post-illumination photoconductivity enables extension of photo-catalysis after sunset, *Adv. Energy Mater.* 11 (2021) 2101566.
- [14] N. Zhang, C. Ye, H. Yan, L. Li, H. He, D. Wang, Y. Li, Single-atom site catalysts for environmental catalysis, *Nano Res.* 13 (2020) 3165–3182.
- [15] H. Zhu, C. Chen, X. Chen, S. Feng, B. Li, Y. Du, G. Liu, H.M. Cheng, Patterning alternate TiO<sub>2</sub> and Cu<sub>2</sub>O strips on conductive substrate as film photocatalyst for Z-scheme photocatalytic water splitting, *Sci. Bull.* 67 (2022) 2420–2427.
- [16] T.W. Kim, K.S. Choi, Nanoporous BiVO<sub>4</sub> photoanodes with dual-layer oxygen evolution catalysts for solar water splitting, *Science* 343 (2014) 990–994.
- [17] V. Andrei, G.M. Ucoski, C. Pornrungraj, C. Uswachoke, Q. Wang, D.S. Achilleos, H. Kasap, K.P. Sokol, R.A. Jagt, H. Lu, T. Lawson, A. Wagner, S.D. Pike, D.S. Wright, R.L.Z. Hoye, J.L. MacManus-Driscoll, H.J. Joyce, R.H. Friend, E. Reisner, Floating perovskite-BiVO<sub>4</sub> devices for scalable solar fuel production, *Nature* 608 (2022) 518–522.
- [18] L. Jiao, H.L. Jiang, Metal-organic frameworks for catalysis: fundamentals and future prospects, *Chin. J. Catal.* 45 (2023) 1–5.
- [19] Y. Xing, S. Liu, Recent progress in  $\pi$ -conjugated polymer-inorganic heterostructures for photocatalysis, *Chin. J. Struct. Chem.* 41 (2022) 2209056–2209068.
- [20] W. Zhou, Q. Jing, J. Li, Y. Chen, G. Hao, L.N. Wang, Organic photocatalysts for solar water splitting: molecular- and aggregate-level modifications, *Acta Phys. Chim. Sin.* 39 (2023) 2211010.
- [21] L.L. Zheng, L.S. Zhang, Y. Chen, L. Tian, X.H. Jiang, L.S. Chen, Q.J. Xing, X.Z. Liu, D.S. Wu, J.P. Zou, A new strategy for the fabrication of covalent organic framework-metal-organic framework hybrids via in-situ functionalization of ligands for improved hydrogen evolution reaction activity, *Chin. J. Catal.* 43 (2022) 811–819.
- [22] X. Sun, L. Sun, G. Li, Y. Tuo, C. Ye, J. Yang, J. Low, X. Yu, J.H. Bitter, Y. Lei, D. Wang, Y. Li, Phosphorus tailors the d-band center of copper atomic sites for efficient CO<sub>2</sub> photoreduction under visible-light irradiation, *Angew. Chem. Int. Ed.* 61 (2022) e202207677.
- [23] Z. Luo, X. Ye, S. Zhang, S. Xue, C. Yang, Y. Hou, W. Xing, R. Yu, J. Sun, Z. Yu, X. Wang, Unveiling the charge transfer dynamics steered by built-in electric fields in BiOBr photocatalysts, *Nat. Commun.* 13 (2022) 2230.
- [24] A.M. Ganose, M. Cuff, K.T. Butler, A. Walsh, D.O. Scanlon, Interplay of orbital and relativistic effects in bismuth oxyhalides: BiOF, BiOCl, BiOBr, and BiOI, *Chem. Mater.* 28 (2016) 1980–1984.
- [25] Y. Jin, F. Li, T. Li, X. Xing, W. Fan, L. Zhang, C. Hu, Enhanced internal electric field in S-doped BiOBr for intercalation, adsorption and degradation of ciprofloxacin by photoinitiation, *Appl. Catal., B* 302 (2022) 120824.
- [26] M. Shi, G. Li, J. Li, X. Jin, X. Tao, Z. Bin, E.A. Pidko, R. Li, C. Li, Intrinsic facet-dependent reactivity of well-defined BiOBr nanosheets on photocatalytic water splitting, *Angew. Chem. Int. Ed.* 132 (2020) 6652–6657.
- [27] B. Fang, Z. Xing, D. Sun, Z. Li, W. Zhou, Hollow semiconductor photocatalysts for solar energy conversion, *Adv. Powder Mater.* 1 (2022) 100021.
- [28] F.J. Chen, A.S. Gong, M.W. Zhu, G. Chen, S.D. Lacey, F. Jiang, Y.F. Li, Y.B. Wang, J.Q. Dai, Y.G. Yao, J.W. Song, B.Y. Liu, K. Fu, S. Das, L.B. Hu, Mesoporous, three-dimensional wood membrane decorated with nanoparticles for highly efficient water treatment, *ACS Nano* 11 (2017) 4275–4282.
- [29] X. Tao, Y. Zhao, S. Wang, C. Li, R. Li, Recent advances and perspectives for solar-driven water splitting using particulate photocatalysts, *Chem. Soc. Rev.* 51 (2022) 3561–3608.
- [30] D. Zhou, H. Luo, F. Zhang, J. Wu, J. Yang, H. Wang, Efficient photocatalytic degradation of the persistent PET fiber-based microplastics over Pt nanoparticles decorated N-doped TiO<sub>2</sub> nanoflowers, *Adv. Fiber Mater.* 4 (2022) 1094–1107.
- [31] X. Li, T. Liu, Y. Zhang, J. Cai, M. He, M. Li, Z. Chen, L. Zhang, Growth of BiOBr/ZIF-67 nanocomposites on carbon fiber cloth as filter-membrane-shaped photocatalyst for degrading pollutants in flowing wastewater, *Adv. Fiber Mater.* 4 (2022) 1620–1631.
- [32] Y. Wang, Z. Li, W. Fu, Y. Dai, Core-sheath CeO<sub>2</sub>/SiO<sub>2</sub> nanofibers as nanoreactors for stabilizing sinter-resistant Pt, enhanced catalytic oxidation and water remediation, *Adv. Fiber Mater.* 4 (2022) 1278.
- [33] H. Gong, L. Wang, K. Zhou, D. Zhang, Y. Zhang, V. Adamaki, C. Bowen, A. Sergejevs, Improved photocatalytic performance of gradient reduced TiO<sub>2</sub> ceramics with aligned pore channels, *Adv. Powder Mater.* 1 (2022) 100025.
- [34] Y. Li, J. Ma, L. Xu, T. Liu, T. Xiao, D. Chen, Z. Song, J. Qiu, Y. Zhang, Enhancement of charge separation and NIR light harvesting through construction of 2D–2D Bi<sub>4</sub>O<sub>5</sub><sub>2</sub>/BiOBr:Yb<sup>3+</sup>, Er<sup>3+</sup> Z-scheme heterojunctions for improved full-spectrum photocatalytic performance, *Adv. Sci.* 10 (2023) 2207514.
- [35] C. Pornrungraj, A.B.M. Annar, Q. Wang, M. Rahaman, S. Bhattacharjee, V. Andrei, E. Reisner, Hybrid photothermal-photocatalyst sheets for solar-driven overall water splitting coupled to water purification, *Nature Water* 1 (2023) 952–960.
- [36] Y. Zhang, L. Zhang, D. Zeng, W. Wang, J. Wang, W. Wang, W. Wang, An efficient strategy for photocatalytic hydrogen peroxide production over oxygen-enriched graphitic carbon nitride with sodium phosphate, *Chin. J. Catal.* 43 (2022) 2690–2698.
- [37] X. Sun, L. Li, S. Jin, W. Shao, H. Wang, X. Zhang, Y. Xie, Interface boosted highly efficient selective photooxidation in Bi<sub>3</sub>O<sub>4</sub>Br/Bi<sub>2</sub>O<sub>3</sub> heterojunctions, *eScience* 3 (2023) 100095.
- [38] Y. Liu, F. Yu, F. Wang, S. Bai, G. He, Construction of Z-scheme In<sub>2</sub>S<sub>3</sub>-TiO<sub>2</sub> for CO<sub>2</sub> reduction under concentrated natural sunlight, *Chin. J. Struct. Chem.* 41 (2022) 2201034–2201039.
- [39] Z. Liang, Y. Xue, X. Wang, X. Zhang, J. Tian, H. Cui, The incorporation of cocatalyst cobalt sulfide into graphitic carbon nitride: boosted photocatalytic hydrogen evolution performance and mechanism exploration, *Nano Mater. Sci.* 5 (2023) 202–209.
- [40] J. Zhang, Z. Pan, Y. Yang, P. Wang, C. Pei, W. Chen, G. Huang, Boosting the catalytic activity of a step-scheme In<sub>2</sub>O<sub>3</sub>/ZnIn<sub>2</sub>S<sub>4</sub> hybrid system for the photofixation of nitrogen, *Chin. J. Catal.* 43 (2022) 265–275.
- [41] C. Wang, C. You, K. Rong, C. Shen, Y. Fang, S. Li, An S-scheme MIL-101(Fe)-on-BiOCl heterostructure with oxygen vacancies for boosting photocatalytic removal of Cr(VI), *Acta Phys. Chim. Sin.* 40 (2024) 2307045.
- [42] S. Li, K. Dong, M. Cai, X. Li, X. Chen, A plasmonic S-scheme Au/MIL-101(Fe)/BiOBr photocatalyst for efficient synchronous decontamination of Cr(VI) and norfloxacin antibiotic, *eScience* 4 (2024) 100208.
- [43] S. Li, C. Wang, K. Dong, P. Zhang, X. Chen, X. Li, MIL-101(Fe)/BiOBr S-scheme photocatalyst for promoting photocatalytic abatement of Cr(VI) and enrofloxacin antibiotic: performance and mechanism, *Chin. J. Catal.* 51 (2023) 101–112.
- [44] Z. Zhao, J. Bian, L. Zhao, H. Wu, S. Xu, L. Sun, Z. Li, Z. Zhang, L. Jing, Construction of 2D Zn-MOF/BiVO<sub>4</sub> S-scheme heterojunction for efficient photocatalytic CO<sub>2</sub> conversion under visible light irradiation, *Chin. J. Catal.* 43 (2022) 1331–1340.
- [45] Z. Wang, B. Cheng, L. Zhang, J. Yu, Y. Li, S. Wageh, A.A. Al-Ghamdi, S-scheme 2D/2D Bi<sub>2</sub>MoO<sub>6</sub>/BiOI van der Waals heterojunction for CO<sub>2</sub> photoreduction, *Chin. J. Catal.* 43 (2022) 1657–1666.
- [46] X. Wu, G. Chen, J. Wang, J. Li, G. Wang, Review on S-scheme heterojunctions for photocatalytic hydrogen evolution, *Acta Phys. Chim. Sin.* 39 (2023) 2212016.
- [47] B. Huang, X. Fu, K. Wang, L. Wang, H. Zhang, Zhongyi Liu, B. Liu, J. Li, Chemically bonded BiVO<sub>4</sub>/Bi<sub>19</sub>Cl<sub>3</sub>S<sub>27</sub> heterojunction with fast hole extraction dynamics for continuous CO<sub>2</sub> photoreduction, *Adv. Powder Mater.* 3 (2024) 100140.
- [48] K. Dong, C. Shen, R. Yan, Y. Liu, C. Zhuang, S. Li, Integration of plasmonic effect and S-scheme heterojunction into Ag/Ag<sub>3</sub>Po<sub>4</sub>/C<sub>3</sub>N<sub>5</sub> photocatalyst for boosted photocatalytic levofloxacin degradation, *Acta Phys. Chim. Sin.* 40 (2024) 2310013.
- [49] X. Wang, X. Wang, J. Huang, S. Li, A. Meng, Z. Li, Interfacial chemical bond and internal electric field modulated Z-scheme Sv-ZnIn<sub>2</sub>S<sub>4</sub>/MoSe<sub>2</sub> photocatalyst for efficient hydrogen evolution, *Nat. Commun.* 12 (2021) 4112.
- [50] L. Zhang, J. Zhang, H. Yu, J. Yu, Emerging S-scheme photocatalyst, *Adv. Mater.* 34 (2022) 2107668.
- [51] X. Zhang, Y. Song, X. Niu, X. Lin, S. Zhong, H. Lin, B. Teng, S. Bai, Emerging hollow artificial photosynthetic system with S-scheme heterojunction sandwiched between layered redox cocatalysts for overall CO<sub>2</sub> reduction and H<sub>2</sub>O oxidation, *Appl. Catal., B* 342 (2024) 123445.
- [52] L. Sun, X. Yu, L. Tang, W. Wang, Q. Liu, Hollow dodecahedron K<sub>3</sub>PW<sub>12</sub>O<sub>40</sub>/CdS core-shell S-scheme heterojunction for photocatalytic synergistic H<sub>2</sub> evolution and benzyl alcohol oxidation, *Chin. J. Catal.* 52 (2023) 164–175.
- [53] H. Jiang, L. Wang, X. Yu, L. Sun, J. Li, J. Yang, Q. Liu, Precise regulation of built-in electric field over NH<sub>2</sub>-MIL-125-Ti<sub>x</sub>WO<sub>3-x</sub> S-scheme heterojunction for achieving simultaneous formation of CO and H<sub>2</sub>O<sub>2</sub> from CO<sub>2</sub> and H<sub>2</sub>O, *Chem. Eng. J.* 466 (2023) 143129.
- [54] O. Altan, E. Altintas, S. Alemdar, Ö. Metin, The rational design of a graphitic carbon nitride-based dual S-scheme heterojunction with energy storage ability as a day/night photocatalyst for formic acid dehydrogenation, *Chem. Eng. J.* 441 (2022) 136047.
- [55] M. Cai, Y. Liu, K. Dong, X. Chen, S. Li, Floatable S-scheme Bi<sub>2</sub>WO<sub>6</sub>/C<sub>3</sub>N<sub>5</sub>/carbon fiber cloth composite photocatalyst for efficient water decontamination, *Chin. J. Catal.* 52 (2023) 239–251.
- [56] Y. Liu, Z. Wang, L. Yao, L. Shi, Simple preparation of amorphous nickel boride/Mn<sub>0.5</sub>Cd<sub>0.5</sub>S composite and its high-efficient photocatalytic performance for hydrogen production, *Sol. Energy* 247 (2022) 177–184.
- [57] J. Xu, M. Zhang, X. Li, M. Chen, Efficient photocatalytic performance of direct Z-scheme photocatalyst Bi<sub>3</sub>TaO<sub>7</sub>/Mn<sub>0.5</sub>Cd<sub>0.5</sub>S for levofloxacin degradation under visible light irradiation, *J. Environ. Chem. Eng.* 10 (2022) 107484.
- [58] H. Peng, C. Huang, X. Zheng, J. Wen, Efficient solar-light photocatalytic H<sub>2</sub> evolution of Mn<sub>0.5</sub>Cd<sub>0.5</sub>S coupling with S, N-codoped carbon, *J. Ind. Eng. Chem.* 106 (2022) 225–232.

- [59] Y. Liu, L. Wang, H. Lv, X. Wu, X. Xing, S. Song, Constructing robust  $\text{MoO}_2/\text{Au}/\text{Mn}_{0.5}\text{Cd}_{0.5}\text{S}$  multiple heterojunctions for improved photocatalytic hydrogen evolution: an insight into the synergistic effect of  $\text{MoO}_2$  and  $\text{Au}$  cocatalysts, *Appl. Surf. Sci.* 541 (2021) 148582.
- [60] Q. Zhang, Z. Wang, Y. Song, J. Fan, T. Sun, E. Liu, S-scheme regulated  $\text{Ni}_2\text{P}-\text{NiS}/\text{twinned Mn}_{0.5}\text{Cd}_{0.5}\text{S}$  hetero-homojunctions for efficient photocatalytic  $\text{H}_2$  evolution, *J. Mater. Sci. Technol.* 169 (2024) 148–157.
- [61] Y. Chen, H. Tian, W. Zhu, X. Zhang, R. Li, C. Chen, Y. Huang, L-cysteine directing synthesis of BiOBr nanosheets for efficient cefazolin photodegradation: the pivotal role of thiol, *J. Hazard Mater.* 414 (2021) 125544.
- [62] Z. Li, D. Lan, Z. Li, J. Sun, S. Chen, J. Yang, J. Wei, Z. Yu, S. Wang, Y. Hou, Step-doped disulfide vacancies and functional groups synergistically enhance photocatalytic activity of S-scheme  $\text{Cu}_3\text{SnS}_4/\text{L-BiOBr}$  towards ciprofloxacin degradation, *Chemosphere* 301 (2022) 134684.
- [63] J. Zhao, M. Xue, M. Ji, B. Wang, Y. Wang, Y. Li, Z. Chen, H. Li, J. Xia, "Electron collector"  $\text{Bi}_{19}\text{S}_{27}\text{Br}_3$  nanorod-enclosed BiOBr nanosheet for efficient  $\text{CO}_2$  photoconversion, *Chin. J. Catal.* 43 (2022) 1324–1330.
- [64] S. Bai, H. Qiu, M. Song, G. He, F. Wang, Y. Liu, L. Guo, Porous fixed-bed photoreactor for boosting C–C coupling in photocatalytic  $\text{CO}_2$  reduction, *eScience* 2 (2022) 428–437.
- [65] N. Zhao, J. Peng, J. Wang, M. Zhai, Novel carboxy-functionalized PVP-CdS nanopopcorns with homojunctions for enhanced photocatalytic hydrogen evolution, *Acta Phys. Chim. Sin.* 38 (2022) 2004046.
- [66] V.T. Huong, B.V. Duc, N.T. An, T.T.P. An, T.M. Aminabhavi, Y. Vasheghian, S.-W. Joo, 3D-Printed  $\text{WO}_3-\text{UiO}-66@\text{reduced graphene oxide}$  nanocomposites for photocatalytic degradation of sulfamethoxazole, *Chem. Eng. J.* 483 (2024) 149277.
- [67] K. Wang, X. Feng, Y. Shangguan, X. Wu, H. Chen, Selective  $\text{CO}_2$  photoreduction to  $\text{CH}_4$  mediated by dimension matched 2D/2D  $\text{Bi}_3\text{NbO}_7/\text{g-C}_3\text{N}_4$  S-scheme heterojunction, *Chin. J. Catal.* 43 (2022) 246–254.
- [68] Z. Miao, Q. Wang, Y. Zhang, L. Meng, X. Wang, In situ construction of S-scheme AgBr/BiOBr heterojunction with surface oxygen vacancy for boosting photocatalytic  $\text{CO}_2$  reduction with  $\text{H}_2\text{O}$ , *Appl. Catal., B* 301 (2022) 120802.
- [69] E. Pastor, M. Sachs, S. Selim, J.R. Durrant, A. Bakulin, A. Walsh, Electronic defects in metal oxide photocatalysts, *Nat. Rev. Mater.* 7 (2022) 503–521.
- [70] G. Ren, M. Shi, Z. Li, Z. Zhang, X. Meng, Electronic metal-support interaction via defective-induced platinum modified BiOBr for photocatalytic  $\text{N}_2$  fixation, *Appl. Catal., B* 327 (2023) 122462.
- [71] Y. Shi, J. Li, D. Huang, X. Wang, Y. Huang, C. Chen, R. Li, Specific adsorption and efficient degradation of cylindrospermopsin on oxygen-vacancy sites of BiOBr, *ACS Catal.* 13 (2022) 445–458.
- [72] J. Guo, X. Li, J. Liang, X.Z. Yuan, L. Jiang, H. Yu, H. Sun, Z. Zhu, S. Ye, N. Tang, J. Zhang, Fabrication and regulation of vacancy-mediated bismuth oxyhalide towards photocatalytic application: development status and tendency, *Coord. Chem. Rev.* 443 (2021) 214033.



**Dr. Shijie Li** received his Ph.D. degree in Environmental Engineering from Donghua University in 2014. He is currently an associate professor at National Engineering Research Center for Marine Aquaculture, Zhejiang Ocean University. His research interests focus on design and synthesis of functional nanomaterials for solar energy conversion and environmental remediation.



**Dr. Xiaobo Chen** is currently a Professor of Chemistry at the University of Missouri – Kansas City (UMKC). He joined UMKC at 2011 after worked in University of California- Berkeley & Berkeley National Laboratory following his Ph.D. at Case Western Reserve University in 2005. He obtained a B.S. from Peking University and M.S. from Dalian Institute of Chemical Physics. He has published about 203 articles from UMKC with about 60,000 citations and an H-index of 75. His research interests are nanomaterials for renewable energy ( $\text{H}_2$  production,  $\text{CO}_2$  reduction, etc) and sustainable environment (pollution removal, etc) towards a better future.



**Dr. Bin Zhang** is a professor worked at College of Food Science and pharmacy, Zhejiang Ocean University, China. His scientific research items include the freshness and quality of marine species, controlling technology of bacteria in aquatic products and advanced functional materials for water purification and disinfection. He has published more than 175 academic papers in the international journals.